Nano Research

Open Access

Research Article

An all-in-one polymer electrolyte enabled by acrylate-grafted separator copolymerization for high-performance lithium metal batteries

Jie Liu[1,3], Jinping Zhang[1,3], Yansong Liu[1,3], Ruiqi Zhao[1,3], Nuo Xu[1,3], Xingchen Song[1,3], Yuhu Li[1,3], Guolin Sun[1,3], Yanfeng Ma[1,3], Chenxi Li[1,3], Hongtao Zhang[1,3], and Yongsheng Chen[1,2,3] ✉

[1] *The Centre of Nanoscale Science and Technology and Key Laboratory of Functional Polymer Materials, Institute of Polymer Chemistry, College of Chemistry, Nankai University, Tianjin 300071, China*
[2] *State Key Laboratory of Elemento-Organic Chemistry, Nankai University, Tianjin 300071, China*
[3] *Renewable Energy Conversion and Storage Center (RECAST), Nankai University, Tianjin 300071, China*

Cite this article: *Nano Research*, **2025**, *18*, 94907323. https://doi.org/10.26599/NR.2025.94907323

ABSTRACT: Polymer electrolytes featuring flexibility, processability, and compatibility with large-scale roll-to-roll fabrication processes have emerged as promising candidates for solid-state lithium metal batteries. Herein, we have designed and synthesized an all-in-one free-standing acrylate-grafted cellulose separator polymer electrolyte (ACSPE) through the copolymerization of acrylate-grafted cellulose separator (ACS). This synthetic strategy leverages the abundant hydroxyl groups in the cellulose separator, which are substituted with acryloyl chloride to form an acrylate-grafted separator. The resulting ACSPE exhibits a high ionic conductivity of 1.78 × 10^{-3} S·cm^{-1} at room temperature, improved oxidation stability (5.57 V), and enhanced mechanical strength (10.0 MPa), indicating its high compatibility with high-voltage cathode, Li metal anode, and scalable roll-to-roll production processes. Li|ACSPE|$LiNi_{0.8}Co_{0.1}Mn_{0.1}O_2$ (NCM811) cells exhibit a long stable cycle life of 1000 cycles at 0.5 C/1 C with capacity retention of 75.6%, achieving stable performance across a wide temperature range from 0 to 60 °C. Furthermore, when paired with a 50 μm thin Li foil, full cells using NCM811 cathode with a mass loading of 6 mg·cm^{-2} exhibit a high discharge capacity of 191.0 mAh·g^{-1} at 0.1 C and maintain excellent cycling stability with a retention rate of 93.3% after 100 cycles. This study provides valuable insights into the chemical modification and design strategies for improving the processability and performance of polymer-based solid-state batteries.

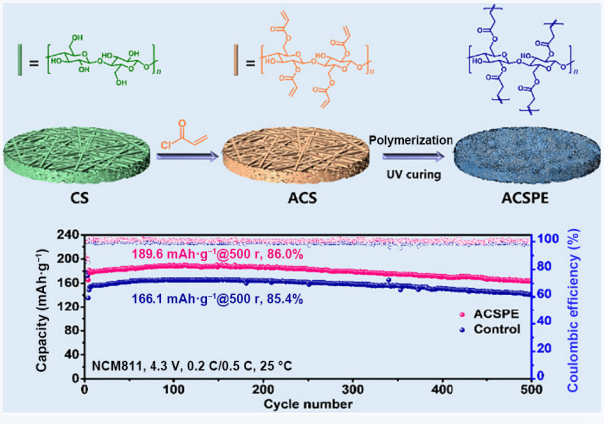

KEYWORDS: polymer electrolytes, lithium metal batteries, high-voltage, long cycling

1 Introduction

Lithium-ion batteries (LIBs) have been widely employed in portable electronic devices, electric vehicles, and large-scale energy storage systems [1, 2]. However, their relatively low energy density (~ 300 Wh·kg^{-1}) presents significant challenges in meeting the escalating demands for higher-performance energy storage solutions [3–5]. In contrast, lithium metal batteries (LMBs), when paired with nickel-rich cathodes, are considered as promising alternatives due to their ability to deliver a significantly enhanced energy density of over 500 Wh·kg^{-1} [6, 7]. Despite their advantages, the application of commercial liquid electrolytes (LEs) in LMBs raises critical safety concerns. These electrolytes are highly flammable and volatile, making them susceptible to fire and explosion hazards [8, 9]. Additionally, the high reactivity of the lithium-metal anode exacerbates issues such as excessive electrolyte consumption and uncontrollable Li-dendrite growth. These challenges not only severely limit the cycle life of the batteries but also lead to short circuits, increasing the risk of catastrophic safety accidents [10, 11].

Solid state electrolytes (SSEs) have emerged as a promising alternative to address the aforementioned issues [12–16]. Among

Received: January 10, 2025; **Revised:** February 18, 2025
Accepted: February 21, 2025

✉Address correspondence to yschen99@nankai.edu.cn

various types of SSEs, inorganic solid electrolytes exhibit excellent ionic conductivity. However, their poor mechanical and interfacial properties, along with challenges in scaling up production, significantly limit their practical applications [17, 18]. In contrast, solid polymer electrolytes (SPEs) offer advantages, such as light weight, excellent flexibility, good processability, and low interfacial resistance, making them highly suitable for integration into solid-state LMBs and large-scale roll-to-roll manufacturing processes [19–23]. Despite these advantages, the ionic conductivities of SPEs at room temperature (~ 10^{-5} S·cm^{-1}) remain relatively low, falling short of the requirement for electrolytes of LMBs [24–27]. To overcome this limitation, one effective method is the incorporation of plasticizers or liquid electrolytes, resulting in the development of quasi-solid polymer electrolytes (QSPEs) or gel polymer electrolytes (GPEs), which exhibit enhanced ionic conductivity [28–30].

Incorporating plasticizers or liquid electrolytes into polymer electrolytes typically compromises their mechanical strength, resulting in short circuiting of batteries during assembly and operation [31]. To address this issue, various strategies have been explored to enhance the mechanical properties of polymer electrolytes [21]. One effective approach involves the creation of chemically cross-linked structure through ultraviolet (UV) or thermal polymerization, which significantly improves mechanical properties [32–34]. Another efficient strategy is the incorporation of a robust porous substrate as a reinforcing framework to strengthen the mechanical properties of polymer electrolytes. Numerous materials have been employed as the substrate in polymer electrolytes, such as polypropylene (PP) separators [35], polyimide (PI) films [36], polyethylene terephthalate (PET) nonwovens [29], porous cellulose nanopaper [37], and so forth. Among them, cellulose-based materials stand out due to their abundant hydroxyl groups, which offer excellent potential for functionalization. This unique property enables the introduction of specialized functionalities or even chemically cross-linked structures, further enhancing their applicability in polymer electrolytes.

In this work, we have successfully developed an all-in-one free-standing acrylate-grafted cellulose separator polymer electrolyte (ACSPE) through the copolymerization of acrylate-grafted cellulose separator (ACS) with polymer monomer and a cross-linker, along with the incorporation of plasticizers. The cellulose separator serves not only as a structural framework but also as a chemically active component that bonds with polymer monomer to form a chemically cross-linked structure. By integrating these two strategies, ACSPE shows enhanced mechanical strength of 10.0 MPa and an expanded electrochemical window of 5.57 V, achieving superior compatibility with both the lithium metal anode and the high-voltage cathode. The fabricated polymer electrolyte exhibits a high ionic conductivity of 1.78 × 10^{-3} S·cm^{-1} at room temperature. Li||Li symmetric cells using ACSPE achieve stable lithium plating/stripping and a prolonged cycling lifespan of 1400 h. Furthermore, Li|ACSPE|$LiNi_{0.8}Co_{0.1}Mn_{0.1}O_2$ (NCM811) batteries deliver a high discharge specific capacity of 189.6 mAh·g^{-1} at 0.5 C and a remarkable cycle life of 1000 cycles at 0.5 C/1 C (charge at 0.5 C and discharge at 1 C), with a capacity retention of 75.6%. Additionally, Li||NCM811 batteries maintain stable performance across a wide temperature range from 0 to 60 °C. At the cut-off voltage of 4.5 V, Li|ACSPE|NCM811 batteries exhibit a high discharge capacity of 207.6 mAh·g^{-1} at 0.5 C and a capacity retention of 80.0% after 300 cycles. The full cells using NCM811 cathode with a mass loading of 6 mg·cm^{-2} and 50 μm Li foil deliver a high discharge capacity of 191.0 mAh·g^{-1} at 0.1 C and excellent cycling stability with a retention rate of 93.3% after 100 cycles. Moreover, the all-in-one polymer electrolytes are compatible with the current roll-to-roll manufacturing process and can be fabricated on an industrial scale. This work offers new perspectives for the chemical modification and large-scale production of polymer-based high-voltage LMBs, offering a promising pathway for their practical application.

2 Results and discussion

2.1 Preparation and characterization of ACSPE

As depicted in Scheme 1, the synthesis initiated with the modification of cellulose separator (CS), which contained abundant hydroxyl groups, through an acylation reaction with acryloyl chloride (AC) to produce an acrylate-grafted cellulose separator. The detailed synthesis procedure is described in Section S1 and Fig. S1 in the Electronic Supplementary Material (ESM). The successful acylation of ACS was confirmed by Fourier transform infrared spectroscopy (FTIR) (Fig. S2 in the ESM), which revealed distinctive adsorption peaks at 1652 and 1716 cm^{-1}, corresponding to C=C and C=O vibrations, respectively. Scanning electron microscopy (SEM) analysis demonstrated that ACS maintained its porous fiber membrane structure (Fig. S3(a) in the ESM), showing

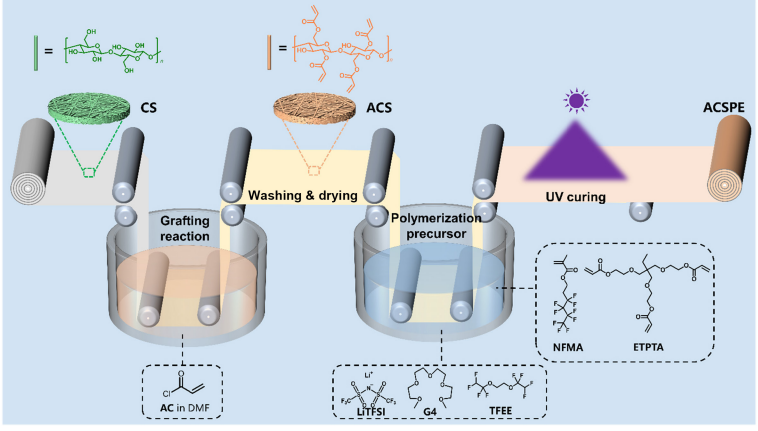

Scheme 1 Schematic diagram of the roll-to-roll continuous coating fabrication process, which consists of four key steps: grafting reaction, washing and drying, dip-coating with precursor, and UV curing.

minimal morphological changes compared to the pristine CS (Fig. S3(b) in the ESM). Following washing and drying procedures, ACSPE was prepared through UV-initiated copolymerization. This process involved the integration of ACS with the monomer (1H,1H,2H,2H-nonafluorohexyl methacrylate, NFMA) and the cross-linker (ethoxylated trimethylolpropane triacrylate, ETPTA) under UV irradiation, along with the addition of lithium salt and plasticizers. The formulation also incorporated lithium bis(trifluoromethanesulfonyl)imide (LiTFSI) as the lithium salt, along with tetraethylene glycol dimethyl ether (G4) and 1,2-bis(1,1,2,2-tetrafluoroethoxy)ethane (TFEE) as plasticizers. The ratio of lithium salt to plasticizers is detailed in Section S1 in the ESM. Furthermore, the successful fabrication of a large-size polymer membrane as shown in Fig. 1(a) demonstrates the feasibility of industrial-scale roll-to-roll manufacturing for ACSPE. For comparison, a control polymer electrolyte (CSPE) was synthesized using pristine cellulose separator without acrylate grafting.

After curing, as shown in the SEM image in Fig. 1(b), ACSPE exhibits a uniform and smooth surface, with polymers thoroughly penetrating the membrane's porous structure. Cross-sectional SEM analysis in Fig. 1(c) indicates that the ACSPE membrane maintains a consistent thickness of approximately 100 μm. To verify the chemical reactions during the UV curing stage, FTIR was conducted. As shown in Fig. 1(d), the disappearance of the C=C adsorption peak at 1645 cm^{-1}, along with the appearance of the distinct C=O vibration peak at 1732 cm^{-1} in ACSPE, confirms the complete polymerization of all components, with a cross-linked polymer network constructed. This cross-linked structure of ACSPE provides a stable framework for the incorporation of plasticizers and lithium salts, thereby facilitating efficient Li^+ transport.

Figure 1(e) presents the X-ray diffraction (XRD) data of CS, ACS, and ACSPE, showing attenuated crystal peaks of ACSPE after polymerization. This attenuation indicates a transition to a more amorphous state, which generally facilitates Li^+ transport and improves the ionic conductivity of the electrolyte [29]. The mechanical properties of polymer electrolytes are crucial for practical application, as they must withstand stresses during battery manufacturing, charge–discharge cycles, and potential mechanical abuses [36]. Notably, ACSPE exhibits a high tensile strength of 10.0 MPa in Fig. 1(f), which is significantly greater than that of CSPE (3.3 MPa). This superior mechanical strength is primarily attributed to the copolymerization of ACS with the polymer skeleton. Additionally, thermogravimetric analysis (Fig. S4 in the ESM) confirms the excellent thermal stability of ACSPE, making it suitable for practical batteries.

Electrochemical impedance spectroscopy (EIS) tests were conducted to evaluate the ionic conductivities of ACSPE at various temperatures, as depicted in Fig. S5 in the ESM. The ionic conductivity of ACSPE attains 1.78×10^{-3} $S \cdot cm^{-1}$ at room temperature. Based on the Arrhenius equation, the activation energy of ACSPE was calculated to be 0.344 eV (Fig. 1(g)), suggesting favorable Li^+ migration kinetics within the electrolyte matrix. Li^+ transference number of Li||Li symmetric cells assembled with ACSPE and CSPE was also evaluated as shown in Fig. S6 in the ESM. To evaluate the electrochemical stability of the electrolytes, linear sweep voltammetry (LSV) measurements were employed to evaluate the electrochemical stability window of the electrolytes. As shown in Fig. 1(h), ACSPE exhibits an electrochemical stability window up to 5.57 V, surpassing that of CSPE (5.08 V). This enhanced oxidation stability is attributed to the copolymerization of ACS within the polymer network, which improves both the structural integrity and electrochemical properties of the electrolyte system.

2.2 Li metal anode stability evaluation

To investigate the compatibility of the electrolyte with lithium metal, Li||Li symmetric cells assembled with ACSPE and CSPE were tested at a current density of 0.1 $mA \cdot cm^{-2}$ and a fixed capacity of 0.1 $mAh \cdot cm^{-2}$ (Fig. 2(a)). The Li|ACSPE|Li cells demonstrated excellent stability in voltage polarization, operating without short-circuiting for over 1400 h. In stark contrast, the control Li|CSPE|Li cell failed due to short-circuiting after merely 291 h of operation. Further testing of Li||Li symmetric cells under more demanding current conditions, as illustrated in Fig. 2(b) and Fig. S7 in the ESM, reveals that the Li|ACSPE|Li cells maintain their stable performance. Notably, the Li|ACSPE|Li cell exhibits a high critical current density (CCD) value of 1.0 $mA \cdot cm^{-2}$, significantly

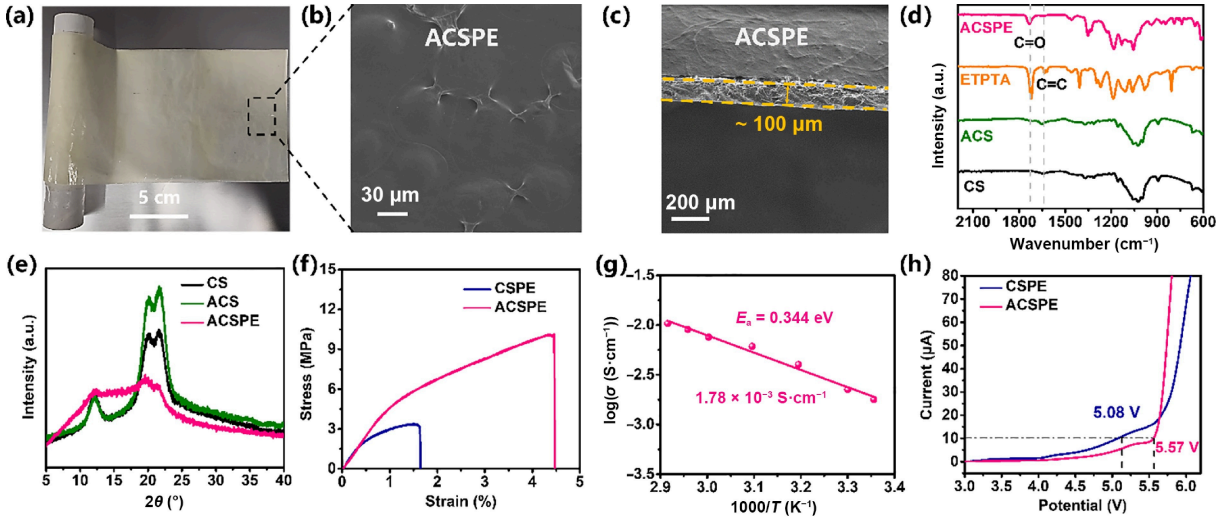

Figure 1 (a) Digital photograph of ACSPE membrane after UV curing. (b) Surface SEM image of ACSPE membrane. (c) Cross-sectional SEM image of ACSPE. (d) FTIR spectra of CS, ACS, ETPTA, and ACSPE. (e) XRD patterns of CS, ACS, and ACSPE. (f) Stress–strain curves of CSPE and ACSPE membranes. (g) Ionic conductivities of ACSPE at different temperatures. (h) LSV curves of the electrolytes at a scan rate of 1 $mV \cdot s^{-1}$ in the voltage range of 3–6 V.

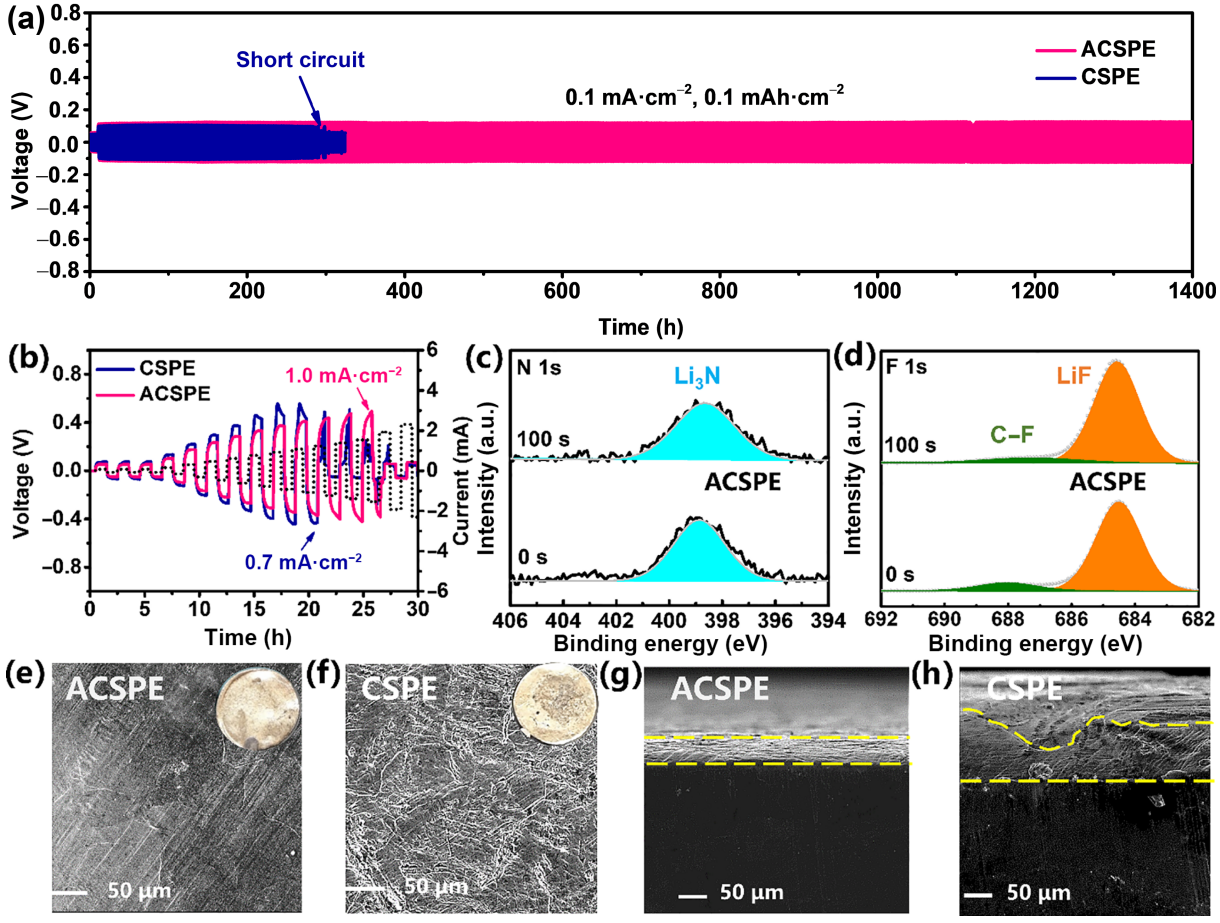

Figure 2 (a) Galvanostatic cycling curves of Li||Li symmetric cells with ACSPE and CSPE at 0.1 mA·cm^{-2} and 0.1 mAh·cm^{-2}. (b) CCD tests of Li|ACSPE|Li and Li|CSPE|Li cells. (c) and (d) XPS depth profiles of N 1s and F 1s for the SEI on the cycled Li metal electrodes with ACSPE. (e)–(h) SEM images illustrating surface morphologies and cross-section views of the Li-metal anodes with ACSPE and CSPE in Li||Li symmetric cells at 0.1 mA·cm^{-2} and 0.1 mAh·cm^{-2} after 50 cycles. Insets of (e) and (f) show digital photographs of the cycled Li metal.

surpassing the CCD of the control CSPE cells, which reaches only 0.7 mA·cm^{-2} (Fig. 2(b)). These results indicate the superior compatibility and enhanced interfacial stability between the ACSPE membrane and the lithium metal anode, underscoring its potential for LMBs.

To elucidate the mechanism underlying the stability between different electrolytes and the lithium metal anode, the compositions of the solid electrolyte interphase (SEI) on the cycled Li metal anode were investigated using X-ray photoelectron spectroscopy (XPS) with Ar ion etching for depth profiling. As depicted in Figs. 2(c) and 2(d) and Fig. S8 in the ESM, the cycled Li metal paired with ACSPE exhibits higher intensities of LiF (684.9 eV) and Li_3N (398.5 eV) species, both on the surface and with increasing sputtering depth. These abundant inorganic species in SEI facilitate uniform Li^+ transport to the Li metal anode surface and significantly suppress Li dendrite growth, thereby enabling stable Li plating/stripping over prolonged cycling [35, 38].

To further evaluate the Li dendrite-suppression capability of different electrolytes, the surface and cross-sectional morphologies of lithium metal electrodes after lithium plating/stripping cycling were characterized by SEM. As presented in Fig. 2(e), the cycled electrode in contact with ACSPE maintains a remarkably uniform and dense surface morphology. In contrast, the electrode paired with CSPE exhibits a porous, rough, and loosely packed surface morphology in Fig. 2(f). These microscopic observations are further corroborated by optical photography. The electrode cycled with CSPE shows significant dead Li formation, evidenced by a distinctive blackened surface, while the ACSPE-paired electrode exhibits minimal dead Li accumulation. This distinction in dead Li formation plays a crucial role in cycling longevity, as excessive dead Li accumulation severely compromises the operational lifespan of the battery. Cross-sectional analyses provide additional insights into the electrode morphologies. The Li metal cycled with ACSPE demonstrates a flat and dense Li deposition pattern in Fig. 2(g), whereas the CSPE-paired Li metal exhibits pronounced protrusions along its cross-section in Fig. 2(h). These results collectively demonstrate the excellent compatibility of the ACSPE with lithium metal anode.

2.3 Electrochemical performance evaluation of high-voltage cathode

The superior anti-oxidative property of ACSPE enables its compatibility with high-voltage cathodes, such as NCM811. To investigate this compatibility, coin cells were assembled using Li metal as the anode, ACSPE and CSPE as electrolytes, and NCM811 as the cathode active material. Figure 3(a) illustrates the cycling performance of Li||NCM811 cells with different electrolytes, with a voltage window of 2.8–4.3 V. The cell using ACSPE exhibits a higher discharge specific capacity of 189.6 mAh·g^{-1} compared to 166.1 mAh·g^{-1} for its CSPE counterpart. Moreover, the ACSPE-

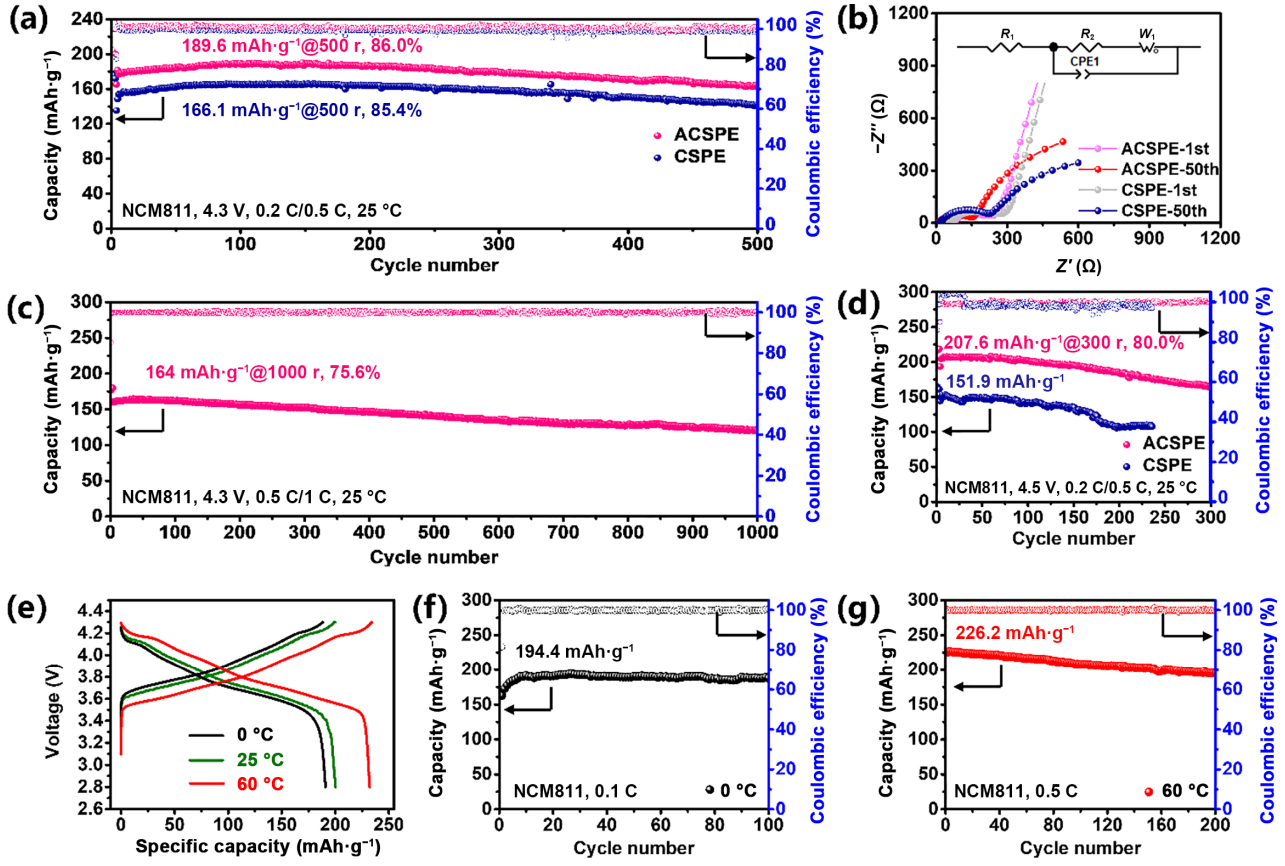

Figure 3 (a) Cycling performance of Li||NCM811 cells with different electrolytes at 0.2 C/0.5 C. (b) Nyquist curves of Li||NCM811 cells with different electrolytes before cycle and after 50 cycles at 0.2 C/0.5 C (inset is the equivalent circuit diagram). (c) Cycling performance of Li|ACSPE|NCM811 cells at 0.5 C/1 C. (d) Cycling performance of 4.5 V Li||NCM811 cells with different electrolytes at 0.2 C/0.5 C. (e) Charge–discharge profiles of Li|ACSPE|NCM811 cell at different temperatures. (f) Cycling performance of Li|ACSPE|NCM811 cell at 0 °C. (g) Cycling performance of Li|ACSPE|NCM811 cell at 60 °C. The mass loading of Li||NCM811 cells is 1.5–2.0 mg·cm^{-2}.

based cells demonstrate significantly improved cycling stability, achieving a higher capacity retention of 86.0% after 500 cycles with a high reversible specific capacity of 162.9 mAh·g^{-1}. To gain deeper insights into the interfacial charge transfer kinetics, we conducted EIS measurements before and after 50 cycles. As shown in Fig. 3(b), the initial EIS results reveal that batteries incorporating ACSPE exhibit lower electrochemical impedance (224 Ω), compared to those with CSPE (268 Ω), indicating enhanced initial ion conduction. After 50 cycles, both systems show decreased impedance values, with ACSPE-based batteries exhibiting a lower impedance of 175 Ω compared to 255 Ω for CSPE-based batteries. These results suggest that ACSPE enables faster ion conduction and establishes improved interfacial contact with electrodes, ultimately leading to enhanced electrochemical performance.

To further investigate the electrochemical stability under elevated current density, Li|ACSPE|NCM811 cells were tested at 0.5 C/1 C using galvanostatic charge/discharge cycling (Fig. 3(c)). The ACSPE-based cell, benefiting from the robust electrode–electrolyte interface provided by the polymer electrolyte, exhibits impressive performance with a high initial discharge capacity of 164 mAh·g^{-1} at 1 C and maintains 75.6% capacity retention after 1000 cycles. Additionally, the ACSPE-based cell also exhibits superior rate performance, delivering remarkable specific capacities of 200.5, 190.7, 185.4, 175.8, and 166.7 mAh·g^{-1} at discharge rates of 0.1, 0.2, 0.5, 1, and 1.5 C, respectively (Fig. S9 in the ESM). Furthermore, leveraging the excellent oxidative stability of ACSPE, we explored its application in high-voltage (≥ 4.5 V) cathode systems. As shown in Fig. 3(d), the 4.5 V Li||NCM811 battery incorporating ACSPE exhibits an impressive discharge capacity of 207.6 mAh·g^{-1} and maintains 80.0% capacity retention after 300 cycles. In contrast, the CSPE-based battery exhibits inferior performance with a lower initial discharge capacity of 151.9 mAh·g^{-1} and suffers from significant capacity degradation, retaining only 70.8% capacity after 236 cycles.

In addition, encouraged by the excellent ion transport capability of ACSPE, the performance of Li|ACSPE|NCM811 cell was further evaluated over a broad temperature range. At 0 and 60 °C, the cells manifest excellent discharge capacities of 190.9 and 232.1 mAh·g^{-1} at 0.1 C, respectively (Fig. 3(e)). Furthermore, at 0 °C, the Li|ACSPE|NCM811 battery exhibits outstanding cycling stability with a high capacity retention of 98.4% after 100 cycles at 0.1 C in Fig. 3(f). At 60 °C, the battery with ACSPE displays a high discharge capacity of 226.2 mAh·g^{-1} at 0.5 C and maintains a high capacity retention of 86.4% after 200 cycles in Fig. 3(g).

To further evaluate the versatility of ACSPE, we conducted comprehensive evaluations using various cathode materials, including $LiFePO_4$ (LFP), $LiNi_{0.6}Mn_{0.2}Co_{0.2}O_2$ (NCM622), and $Li_{1.2}Mn_{0.54}Co_{0.13}Ni_{0.13}O_2$ (LMCNO) cathodes. The Li|ACSPE|LFP battery achieved a long cycling stability of over 1000 cycles with an excellent capacity retention of 78.2% (Fig. S10 in the ESM). In addition, the Li|ACSPE|NCM622 battery at a cut-off voltage of 4.3 V exhibited an initial discharge specific capacity of 160.8 mAh·g^{-1} at 0.5 C, maintaining excellent capacity retention of 80.1% after 1000 cycles (Fig. S11 in the ESM). At an elevated cut-

off voltage of 4.5 V, the Li|ACSPE|NCM622 battery displayed an impressive initial discharge capacity of 183.6 mAh·g^{-1} at 0.5 C, retaining a capacity retention of 78.5% after 500 cycles (Fig. S12 in the ESM). Notably, benefiting from the superior electrochemical stability of ACSPE, the Li|ACSPE|LMCNO battery operated successfully at an even higher cut-off voltage of 4.7 V. This system delivered an outstanding discharge specific capacity of 237.2 mAh·g^{-1} at 0.5 C and maintained stable cycling performance over 100 cycles (Fig. S13 in the ESM). These results, summarized in Table S1 in the ESM, highlight that our all-in-one ACSPE design enables excellent cycling performance across various cathode materials and operating conditions, underscoring its remarkable versatility and practical applicability in diverse LMB configurations.

To assess the practical electrochemical performance and safety features of the all-in-one ACSPE, we conducted comprehensive tests using both coin-type and pouch-type cells. In coin full cell configuration with NCM811 cathode (mass loading: 6 mg·cm^{-2}) and 50 μm Li foil, the battery exhibits an impressive discharge specific capacity of 191.0 mAh·g^{-1} at 0.1 C and excellent cycling stability with a retention rate of 93.3% after 100 cycles (Fig. 4(a)). The system demonstrates robust performance even with increased cathode mass loading of 7.3 mg·cm^{-2}, sustaining stable cycling for 180 cycles (Fig. S14 in the ESM). Meanwhile, the pouch cell displays a high discharge capacity of 192.0 mAh·g^{-1} at 0.2 C with an exceptional capacity retention of 98.8% over 100 cycles (Fig. 4(b)). The charge/discharge curves of 50 μm Li|ACSPE|6.0 mg·cm^{-2} NCM811 coin full cell at 0.1 C and 50 μm Li|ACSPE|2.0 mg·cm^{-2} NCM811 pouch cell at 0.2 C after different cycles are provided in Fig. S15 in the ESM. The performance of 50 μm Li|ACSPE|6.1 mg·cm^{-2} NCM811 pouch full cell at 0.05 C was evaluated, as shown in Fig. S16 in the ESM. It delivers a high discharge capacity of 174.2 mAh·g^{-1} and maintains stable cycling performance over 6 cycles. To further evaluate the safety of the ACSPE electrolyte, we used a pouch cell to power a light-emitting diode (LED) screen displaying the NKU logo as shown in Fig. 4(c) and conducted extreme condition tests. The cell maintains stable operation even under harsh conditions, including bending, cutting, and punching as shown in Figs. 4(d)–4(f). These results demonstrate that the developed all-in-one polymer electrolyte successfully combines its superior safety with excellent electrochemical performance, making it an ideal candidate for practical applications.

2.4 Interfacial behavior of high-voltage cathode

The surface morphologies of high-voltage NCM811 cathodes after 50 cycles in Li||NCM811 batteries with different electrolytes were characterized using SEM. The cycled NCM811 particles from the Li|ACSPE|NCM811 battery display well-preserved mechanical integrity in Fig. 5(a), whereas those from the control Li|CSPE|NCM811 battery show evident intergranular cracking in Fig. 5(b). Such cracking is a well-documented critical issue in Ni-rich cathodes, known to accelerate capacity degradation and severely compromise long-term cycling stability, particularly under high-voltage conditions [39]. Moreover, high-resolution transmission electron microscopy (HRTEM) was employed to investigate the cathode–electrolyte interphase (CEI) morphology and the crystal structure of cycled NCM811 cathodes. In the ACSPE system, a uniform and thin CEI layer with a thickness of ~ 2.6 nm is observed in Fig. 5(c). In contrast, the CSPE system

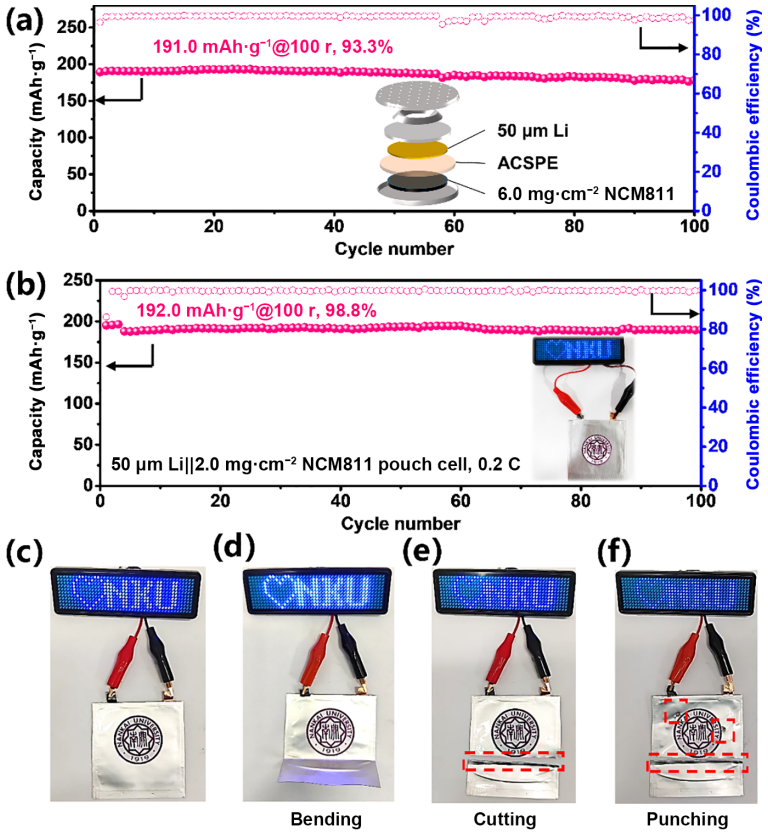

Figure 4 (a) Cycling performances of 50 μm Li|ACSPE|6.0 mg·cm^{-2} NCM811 coin cell at 0.1 C. (b) Cycling performance of Li|ACSPE|NCM811 pouch cell (inset is optical image of pouch cell powering a light-emitting diode screen). (c) Optical image of a pouch cell powering a light-emitting diode screen and optical images of it under harsh conditions including (d) bending, (e) cutting, and (f) punching.

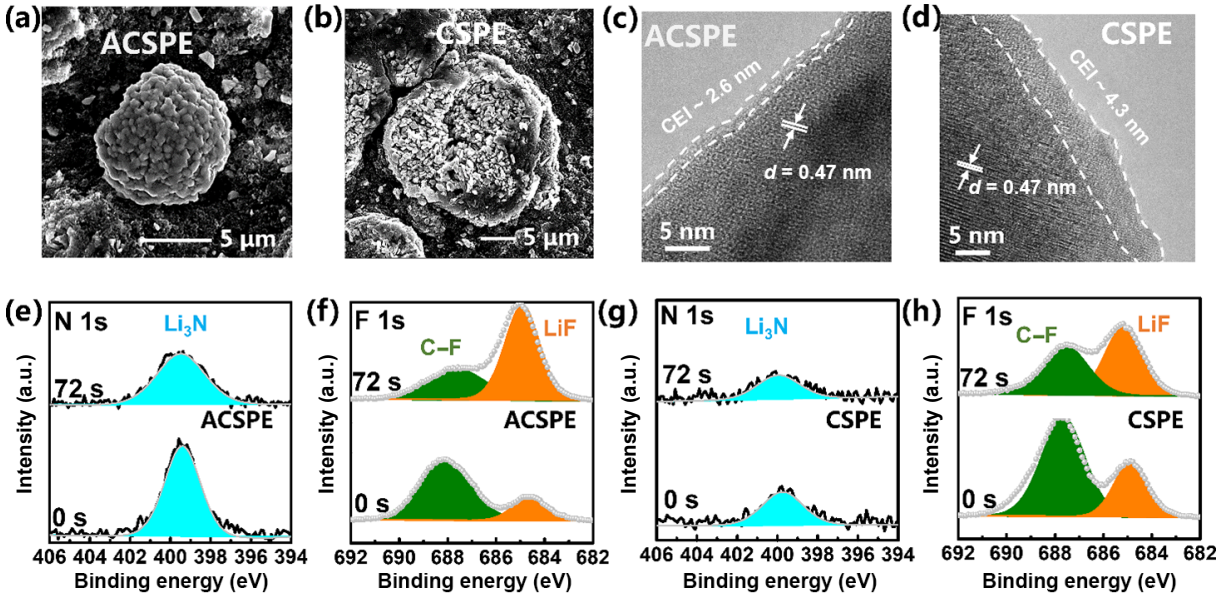

Figure 5 SEM images of the cycled NCM811 cathodes with (a) ACSPE and (b) CSPE after 50 cycles. TEM images of the cycled NCM811 cathodes with (c) ACSPE and (d) CSPE after 50 cycles. (e)–(h) XPS depth profiles of N 1s and F 1s for cycled NCM811 electrodes with ACSPE and CSPE.

develops a thick and non-uniform CEI layer in Fig. 5(d). Moreover, the NCM811 cathode in both systems retains its layered structure with identical lattice spacing of 0.47 nm. The formation of a uniform, thin CEI layer combined with the well-preserved crystal structure provides compelling evidence for the exceptional compatibility between ACSPE electrolyte and high-voltage NCM811 cathodes.

Furthermore, XPS depth profiling was performed to analyze the CEI compositions formed in both electrolytes, as shown in Figs. 5(e)–5(h) and Fig. S17 in the ESM. In the N 1s spectra, the cycled NCM811 with ACSPE in Fig. 5(e) exhibits a higher intensity of Li_3N (398.5 eV) both on the surface and with increasing sputtering depth, compared to the CSPE system in Fig. 5(g). The enhanced presence of Li_3N is beneficial for facilitating uniform Li^+ transport across the interface. Additionally, in the F 1s spectra, as the sputtering depth increases, the intensity of C–F bond of cycled NCM811 with ACSPE decreases while the intensity of LiF increases in Fig. 5(f), which is similar to the CSPE system in Fig. 5(h). But the ACSPE system shows lower intensity of C–F bond compared to the CSPE system. This demonstrates that the surface of NCM811 electrode cycled with ACSPE accumulates fewer side reaction byproducts, efficiently suppressing undesirable interfacial reactions on the cathode surfaces. Further evidence is provided by the C peak analysis, where NCM811 cycled with ACSPE shows notably lower intensity, compared to the CSPE system (Fig. S17 in the ESM). This reduced carbon signal indicates that the CEI formed in ACSPE effectively inhibits solvent consumption, consistent with the observations of a thin and uniform CEI layer. Consequently, these findings elucidate the enhanced electrochemical stability of Li|ACSPE|NCM811 cells during prolonged cycling.

3 Conclusions

In summary, we have successfully developed an innovative all-in-one polymer electrolyte through the chemical bonding of an acrylate-grafted cellulose separator with polymer monomer and a cross-linker. The cellulose separator not only functions as a robust framework but also chemically bonds with polymer monomer to form a chemically cross-linked architecture. As a result, the developed ACSPE exhibits enhanced mechanical strength (10.0 MPa) and an expanded electrochemical window (5.57 V), demonstrating superior compatibility with both the Li metal anode and the high-voltage cathode. In electrochemical performance tests, Li||Li symmetric cells with ACSPE achieved stable Li plating/stripping and demonstrated an extended cycling lifespan for 1400 h. The Li|ACSPE|NCM811 batteries delivered impressive durability, sustaining 1000 cycles at 0.5 C/1 C with capacity retention of 75.6%, while maintaining stable performance across a wide temperature range from 0 to 60 °C. Furthermore, full cells using NCM811 cathode (mass loading: 6 mg·cm^{-2}) and 50 μm Li foil presented a high discharge capacity of 191.0 mAh·g^{-1} at 0.1 C and excellent cycling stability with a retention rate of 93.3% after 100 cycles. A significant advantage of this all-in-one polymer electrolyte lies in its compatibility with existing roll-to-roll manufacturing processes, making it highly suitable for industrial-scale production. This work thus offers valuable insights into the chemical modification and processability design for polymer-based materials, establishing a promising pathway toward the practical implementation of next-generation energy storage systems.

Electronic Supplementary Material: Supplementary material (experimental section, characterizations, electrochemical measurements, and supplementary figures and table) is available in the online version of this article at https://doi.org/10.26599/NR.2025.94907323.

Data availability

All data needed to support the conclusions in the paper are presented in the manuscript and the ESM. Additional data related to this paper may be requested from the corresponding author upon request.

Acknowledgements

The authors gratefully acknowledge the financial support from the

National Natural Science Foundation of China (No. 52090034), the National Key R&D Program of China (No. 2020YFA0711500), and the Beijing–Tianjin–Hebei Basic Research Cooperation Project (No. B24JCZXJC00360).

Declaration of competing interest

All the contributing authors report no conflict of interests in this work.

Author contribution statement

J. L.: Conceptualization, data curation, investigation, methodology, validation, visualization, writing manuscript. J. P. Z.: Data curation. Y. S. L.: Data curation. R. Q. Z.: Data curation. N. X.: Data curation. X. C. S.: Data curation. Y. H. L.: Data curation. G. L. S.: Data curation. Y. F. M.: Supervision, funding acquisition. C. X. L.: Supervision, funding acquisition. H. T. Z.: Methodology, funding acquisition, revising manuscript. Y. S. C.: Conceptualization, supervision, funding acquisition, project administration. All the authors have approved the final manuscript.

Use of AI statement

None.

References

[1] Deng, J.; Bae, C.; Denlinger, A.; Miller, T. Electric vehicles batteries: Requirements and challenges. *Joule* **2020**, *4*, 511–515.

[2] Ni, M. H.; Zhao, Y.; Xu, N.; Kong, M. X.; Ma, Y. F.; Li, C. X.; Zhang, H. T.; Chen, Y. S. Improving the cycling stability of lithium-ion batteries with a dry-processed cathode via the synergistic effect of carboxymethyl cellulose and siloxane. *Sci. China Mater.* **2024**, *67*, 76–84.

[3] Ayyaswamy, A.; Vishnugopi, B. S.; Mukherjee, P. P. Revealing hidden predicaments to lithium-ion battery dynamics for electric vertical take-off and landing aircraft. *Joule* **2023**, *7*, 2016–2034.

[4] Wang, C. Y.; Liu, T.; Yang, X. G.; Ge, S. H.; Stanley, N. V.; Rountree, E. S.; Leng, Y. J.; McCarthy, B. D. Fast charging of energy-dense lithium-ion batteries. *Nature* **2022**, *611*, 485–490.

[5] Choi, J. W.; Aurbach, D. Promise and reality of post-lithium-ion batteries with high energy densities. *Nat. Rev. Mater.* **2016**, *1*, 16013.

[6] Liu, J.; Bao, Z. N.; Cui, Y.; Dufek, E. J.; Goodenough, J. B.; Khalifah, P.; Li, Q. Y.; Liaw, B. Y.; Liu, P.; Manthiram, A. et al. Pathways for practical high-energy long-cycling lithium metal batteries. *Nat. Energy* **2019**, *4*, 180–186.

[7] Janek, J.; Zeier, W. G. Challenges in speeding up solid-state battery development. *Nat. Energy* **2023**, *8*, 230–240.

[8] Feng, X. N.; Ouyang, M. G.; Liu, X.; Lu, L. G.; Xia, Y.; He, X. M. Thermal runaway mechanism of lithium ion battery for electric vehicles: A review. *Energy Storage Mater.* **2018**, *10*, 246–267.

[9] Shi, X. M.; Jia, Z. Z.; Wang, D. H.; Jiang, B. W.; Liao, Y. Q.; Zhang, G. H.; Wang, Q. S.; He, D. Q.; Huang, Y. H. Phonon engineering in solid polymer electrolyte toward high safety for solid-state lithium batteries. *Adv. Mater.* **2024**, *36*, 2405097.

[10] Liu, K.; Liu, Y. Y.; Lin, D. C.; Pei, A.; Cui, Y. Materials for lithium-ion battery safety. *Sci. Adv.* **2018**, *4*, eaas9820.

[11] Yuan, S. Y.; Ding, K.; Zeng, X. Y.; Bin, D.; Zhang, Y. J.; Dong, P.; Wang, Y. G. Advanced nonflammable organic electrolyte promises safer Li-metal batteries: From solvation structure perspectives. *Adv. Mater.* **2023**, *35*, 2206228.

[12] Manthiram, A.; Yu, X. W.; Wang, S. F. Lithium battery chemistries enabled by solid-state electrolytes. *Nat. Rev. Mater.* **2017**, *2*, 16103.

[13] Shi, P. R.; Ma, J. B.; Liu, M.; Guo, S. K.; Huang, Y. F.; Wang, S. W.; Zhang, L. H.; Chen, L. K.; Yang, K.; Liu, X. T. et al. A dielectric electrolyte composite with high lithium-ion conductivity for high-voltage solid-state lithium metal batteries. *Nat. Nanotechnol.* **2023**, *18*, 602–610.

[14] He, F.; Tang, W. J.; Zhang, X. Y.; Deng, L. J.; Luo, J. Y. High energy density solid state lithium metal batteries enabled by sub-5 μm solid polymer electrolytes. *Adv. Mater.* **2021**, *33*, 2105329.

[15] Tang, L. F.; Chen, B. W.; Zhang, Z. H.; Ma, C. Q.; Chen, J. C.; Huang, Y. G.; Zhang, F. R.; Dong, Q. Y.; Xue, G. Y.; Chen, D. Q. et al. Polyfluorinated crosslinker-based solid polymer electrolytes for long-cycling 4.5 V lithium metal batteries. *Nat. Commun.* **2023**, *14*, 2301.

[16] Dai, C.; Stadler, F. J.; Li, Z. M.; Huang, Y. F. E-beam irradiation of poly(vinylidene fluoride-trifluoroethylene) induces high dielectric constant and all-*trans* conformation for highly ionic conductive solid-state electrolytes. *Energy Mater. Devices* **2023**, *1*, 9370016.

[17] Zhang, J. P.; Zhu, J.; Zhao, R. Q.; Liu, J.; Song, X. C.; Xu, N.; Liu, Y. S.; Zhang, H. T.; Wan, X. J.; Ma, Y. F. et al. An all-in-one free-standing single-ion conducting semi-solid polymer electrolyte for high-performance practical Li metal batteries. *Energy Environ. Sci.* **2024**, *17*, 7119–7128.

[18] Yuan, Y.; Chen, L. K.; Li, Y. H.; An, X. F.; Lv, J. S.; Guo, S. K.; Cheng, X.; Zhao, Y.; Liu, M.; He, Y. B. et al. Functional $LiTaO_3$ filler with tandem conductivity and ferroelectricity for PVDF-based composite solid-state electrolyte. *Energy Mater. Devices* **2023**, *1*, 9370004.

[19] Han, S. T.; Wen, P.; Wang, H. J.; Zhou, Y.; Gu, Y.; Zhang, L.; Shao-Horn, Y.; Lin, X. R.; Chen, M. Sequencing polymers to enable solid-state lithium batteries. *Nat. Mater.* **2023**, *22*, 1515–1522.

[20] Zhao, Q. Interphases of polymer electrolytes. *Joule* **2019**, *3*, 1569–1571.

[21] Zhao, Q.; Liu, X. T.; Stalin, S.; Khan, K.; Archer, L. A. Solid-state polymer electrolytes with in-built fast interfacial transport for secondary lithium batteries. *Nat. Energy* **2019**, *4*, 365–373.

[22] Ye, Y. N.; Zhu, X. G.; Meng, N.; Lian, F. Largely promoted mechano-electrochemical coupling properties of solid polymer electrolytes by introducing hydrogen bonds-rich network. *Adv. Funct. Mater.* **2023**, *33*, 2307045.

[23] Du, A.; Lu, H. T.; Liu, S. S.; Chen, S. Y.; Chen, Z. H.; Li, W. H.; Song, J. W.; Yang, Q. H.; Yang, C. P. Breaking the trade-off between ionic conductivity and mechanical strength in solid polymer electrolytes for high-performance solid lithium batteries. *Adv. Energy Mater.* **2024**, *14*, 2400808.

[24] Xue, Z. G.; He, D.; Xie, X. L. Poly(ethylene oxide)-based electrolytes for lithium-ion batteries. *J. Mater. Chem. A* **2015**, *3*, 19218–19253.

[25] Zhao, L. Y.; Dong, Q. Y.; Wang, Y. Q.; Xue, G. Y.; Wang, X. C.; Li, Z. Y.; Shao, H.; Chen, H. W.; Shen, Y. B.; Chen, L. W. Anion modulation: Enabling highly conductive stable polymer electrolytes for solid-state Li-metal batteries. *Angew. Chem., Int. Ed.* **2024**, *63*, e202412280.

[26] Dong, T. T.; Zhang, J. J.; Xu, G. J.; Chai, J. C.; Du, H. P.; Wang, L. L.; Wen, H. J.; Zang, X.; Du, A. B.; Jia, Q. M. et al. A multifunctional polymer electrolyte enables ultra-long cycle-life in a high-voltage lithium metal battery. *Energy Environ. Sci.* **2018**, *11*, 1197–1203.

[27] Zhang, Q. Q.; Liu, K.; Ding, F.; Liu, X. J. Recent advances in solid polymer electrolytes for lithium batteries. *Nano Res.* **2017**, *10*, 4139–4174.

[28] Yang, X. F.; Sun, Q.; Zhao, C. T.; Gao, X. J.; Adair, K. R.; Liu, Y. L.; Luo, J.; Lin, X. T.; Liang, J. N.; Huang, H. et al. High-areal-capacity all-solid-state lithium batteries enabled by rational design of fast ion transport channels in vertically-aligned composite polymer electrodes. *Nano Energy* **2019**, *61*, 567–575.

[29] Qi, S. G.; Li, S. L.; Zou, W. W.; Zhang, W. F.; Wang, X. J.; Du, L.;

Liu, S. M.; Zhao, J. Q. Enabling scalable polymer electrolyte with synergetic ion conductive channels via a two stage rheology tuning UV polymerization strategy. *Small* **2022**, *18*, 2202013.

[30] Sun, Q. F.; Wang, S.; Ma, Y.; Song, D. W.; Zhang, H. Z.; Shi, X. X.; Zhang, N.; Zhang, L. Q. Li-ion transfer mechanism of gel polymer electrolyte with sole fluoroethylene carbonate solvent. *Adv. Mater.* **2023**, *35*, 2300998.

[31] Feng, J. W.; Wang, J. Y.; Gu, Q.; Li, P. T.; Xu, H. L.; Deng, Y. H.; Gao, P. 1 μm-thick robust gel polymer electrolyte with excellent interfacial stability for high-performance Li metal batteries. *Adv. Funct. Mater.* **2024**, *35*, 2412287.

[32] Goujon, L. J.; Khaldi, A.; Maziz, A.; Plesse, C.; Nguyen, G. T. M.; Aubert, P. H.; Vidal, F.; Chevrot, C.; Teyssié, D. Flexible solid polymer electrolytes based on nitrile butadiene rubber/poly(ethylene oxide) interpenetrating polymer networks containing either LiTFSI or EMITFSI. *Macromolecules* **2011**, *44*, 9683–9691.

[33] Oh, S.; Kim, D. W.; Lee, C.; Lee, M. H.; Kang, Y. K. Poly(vinylpyridine-co-styrene) based *in situ* cross-linked gel polymer electrolyte for lithium-ion polymer batteries. *Electrochim. Acta* **2011**, *57*, 46–51.

[34] Lu, Q. W.; He, Y. B.; Yu, Q. P.; Li, B. H.; Kaneti, Y. V.; Yao, Y. W.; Kang, F. Y.; Yang, Q. H. Dendrite-free, high-rate, long-life lithium metal batteries with a 3D cross-linked network polymer electrolyte. *Adv. Mater.* **2017**, *29*, 1604460.

[35] Qi, S. G.; Li, M. R.; Gao, Y. Q.; Zhang, W. F.; Liu, S. M.; Zhao, J. Q.; Du, L. Enabling scalable polymer electrolyte with dual-reinforced stable interface for 4.5 V lithium metal batteries. *Adv. Mater.* **2023**, *35*, 2304951.

[36] Wan, J. Y.; Xie, J.; Kong, X.; Liu, Z.; Liu, K.; Shi, F. F.; Pei, A.; Chen, H.; Chen, W.; Chen, J. et al. Ultrathin, flexible, solid polymer composite electrolyte enabled with aligned nanoporous host for lithium batteries. *Nat. Nanotechnol.* **2019**, *14*, 705–711.

[37] Zhou, K. F.; Zhang, M.; Zhang, X. N.; Wang, T. Y.; Wang, H. L.; Wang, Z. Q.; Tang, X. Y.; Bai, M.; Li, S. W.; Wang, Z. H. et al. A cellulose reinforced polymer composite electrolyte for the wide-temperature-range solid lithium batteries. *Chem. Eng. J.* **2023**, *464*, 142537.

[38] Ji, X.; Hou, S.; Wang, P. F.; He, X. Z.; Piao, N.; Chen, J.; Fan, X. L.; Wang, C. S. Solid-state electrolyte design for lithium dendrite suppression. *Adv. Mater.* **2020**, *32*, 2002741.

[39] Ni, L. S.; Zhang, S.; Di, A. D.; Deng, W. T.; Zou, G. Q.; Hou, H. S.; Ji, X. B. Challenges and strategies towards single-crystalline Ni-rich layered cathodes. *Adv. Energy Mater.* **2022**, *12*, 2201510.